1-1-2012

Radially extended kinematics in the S0 galaxy NGC 2768 from planetary nebulae, globular clusters and starlight

D. A. Forbes
Swinburne University

A. Cortesi
Swinburne University

V. Pota
Swinburne University

C. Foster
European Southern Observatory

Aaron J. Romanowsky
San Jose State University, aaron.romanowsky@sjsu.edu

See next page for additional authors

Recommended Citation

Authors

D. A. Forbes, A. Cortesi, V. Pota, C. Foster, Aaron J. Romanowsky, M. R. Merrifield, J. P. Strader, L. Coccato, and N. Napolitano

Radially extended kinematics in the S0 galaxy NGC 2768 from planetary nebulae, globular clusters and starlight

Duncan A. Forbes,[1]⋆ Arianna Cortesi,[1,2] Vincenzo Pota,[1] Caroline Foster,[3]
Aaron J. Romanowsky,[4] Michael R. Merrifield,[2] Jean P. Brodie,[4]
Jay Strader,[5] Lodovico Coccato[6] and Nicola Napolitano[7]

[1]*Centre for Astrophysics & Supercomputing, Swinburne University, Hawthorn VIC 3122, Australia*
[2]*School of Physics and Astronomy, University of Nottingham, University Park, Nottingham NG7 2RD*
[3]*European Southern Observatory, Alonso de Cordova 3107, Vitacura, Santiago, Chile*
[4]*University of California Observatories, Santa Cruz, CA 95064, USA*
[5]*Harvard-Smithsonian Center for Astrophysics, Cambridge, MA 02138, USA*
[6]*European Southern Observatory, Karl-Schwarzschild-Strasse 2, 85748 Garching, Germany*
[7]*Istituto Nazionale di Astrofisica, Observatorio Astronomico di Capodimonte, Via Moiarello 16, 80131, Naples, Italy*

ABSTRACT

There are only a few tracers available to probe the kinematics of individual early-type galaxies beyond one effective radius. Here we directly compare a sample of planetary nebulae (PNe), globular clusters (GCs) and galaxy starlight velocities out to approximately four effective radii, in the S0 galaxy NGC 2768. Using a bulge-to-disc decomposition of a *K*-band image we assign PNe and starlight to either the disc or the bulge. We show that the bulge PNe and bulge starlight follow the same radial density distribution as the red subpopulation of GCs, whereas the disc PNe and disc starlight are distinct components. We find good kinematic agreement between the three tracers to several effective radii (and with stellar data in the inner regions). Further support for the distinct nature of the two galaxy components comes from our kinematic analysis. After separating the tracers into bulge and disc components we find the bulge to be a slowly rotating pressure-supported system, whereas the disc reveals a rapidly rising rotation curve with a declining velocity dispersion profile. The resulting V_{rot}/σ ratio for the disc resembles that of a spiral galaxy and hints at an origin for NGC 2768 as a transformed late-type galaxy. A two-component kinematic analysis for a sample of S0s will help to elucidate the nature of this class of galaxy.

Key words: galaxies: elliptical and lenticular, cD – galaxies: individual: NGC 2768 – galaxies: kinematics and dynamics.

1 INTRODUCTION

Based on studies of the morphology-density relation in clusters (Dressler 1980) and groups (Wilman et al. 2009), it has been suggested that lenticular (S0) galaxies may be the descendants of spirals that have undergone some evolutionary process (e.g. ram pressure stripping, galaxy harassment, gas starvation and/or mergers). Recent investigations of S0s have studied their metallicity gradients (Bedregal et al. 2011), Tully–Fisher relation (Bedregal, Aragón-Salamanca & Merrifield 2006) and stellar populations (Aragón-Salamanca, Bedregal & Merrifield 2006). However, the origin of S0s is still a subject of much debate (e.g. Kormendy & Bender 2012). The internal kinematics of galaxies are a key tool to un-derstanding their structure and formation histories, and S0s are no exception. For example, the kinematics will be largely unaffected if S0s are formerly spirals that have been simply stripped of gas or if they are involved in a relatively minor merger.

Although half of the stellar mass within a galaxy lies within one effective radius (R_e), more than 90 per cent of the *total* mass and angular momentum does not (Romanowsky & Fall 2012). Thus in order to examine the internal kinematics and total mass of early-type galaxies one must probe well beyond 1 R_e. Elliptical and S0 (early-type) galaxies often lack the significant quantities of extended HI gas commonly found in spirals, so the kinematic tracers are the galaxy starlight themselves, planetary nebulae (PNe) and globular clusters (GCs).

Using the underlying starlight of a galaxy to probe its stellar kinematics is perhaps the preferred method; however, the surface brightness of a galaxy declines rapidly with increasing radius so

⋆E-mail: dforbes@swin.edu.au

it is very difficult to obtain high quality spectra beyond a few effective radii without a large investment of 8-m-class telescope time (Coccato et al. 2010) or using deep single pointings (Weijmans et al. 2009). PNe and GCs have the advantage that they are ubiquitous in the haloes of early-type galaxies out to large galactocentric radii (5–10 R_e). Although there have been several studies of PNe and GC system kinematics in early-type galaxies, very few studies have directly compared them to each other, or to results from galaxy starlight over a common radial range.

Luminous PNe are the end product of low mass stars. However, there is still debate as to whether they arise from normal single-star evolutionary processes or from mass transfer in a binary star system (Ciardullo et al. 2005). In the former case, the PNe observed in early-type galaxies would have an age of ∼1.5 Gyr, and in the latter case they could be as old as 10 Gyr. Coccato et al. (2009) showed that the radial surface density of PNe follows the galaxy starlight in early-type galaxies and that they are useful probes of galaxy kinematics. However, ellipticals with embedded thick discs and S0 galaxies may contain two subpopulations of PNe, one associated with the disc and one with the bulge, as seen for spiral galaxies (Nolthenius & Ford 1987; Hurley-Keller et al. 2004). Not accounting for the different kinematics of these distinct PNe subpopulations could lead to misleading results as illustrated recently by Cortesi et al. (2011) for the lenticular galaxy NGC 1023. Furthermore, Dekel et al. (2005) suggested that an intermediate-aged population of PNe may have 'contaminated' the PNe velocity dispersions of some galaxies in the early-type sample of Romanowsky et al. (2003) and hence impacted the resulting mass analysis.

The globular cluster (GC) systems of all large galaxies, irrespective of Hubble type, generally consist of two subpopulations – blue (or metal-poor) and red (or metal-rich). Both of these subpopulations are thought to have ages ≥10 Gyr and hence trace old stellar populations (for a review of GC system properties see Brodie & Strader 2006). The blue subpopulation is associated with galaxy haloes (Forte et al. 2005; Forbes et al. 2012), whereas the red subpopulation has been shown to share many properties with the spheroid/bulge stars of early-type galaxies (Strader et al. 2011; Forbes et al. 2012), including their kinematics (Pota et al. 2012). We note that the association of red GCs with the bulge and not with a thin disc component extends to spiral galaxies, including our own (Minniti 1995; Côté 1999) and the Sombrero (Forbes, Brodie & Larsen 2001).

To better understand the issues discussed above it is important to directly compare different kinematic tracers for the same galaxy. Here we combine starlight, PNe and GC data for an arche-type lenticular galaxy NGC 2768 and directly compare these different kinematic tracers in the same galaxy. The galaxy is a nearby, near edge-on S0 (Sandage, Tammann & van den Bergh 1981), although we note that it was originally classified as an E6 in the RC3 catalogue. According to Wikland et al. (1995) it is an isolated galaxy; however, it has also been classified as part of the Lyon Group of Galaxies 167 (Garcia 1993). It reveals ionized gas and a minor axis dust lane (Kim 1989). The central ionized gas and stars are known to have different kinematics (Fried & Illingworth 1994) suggesting an external origin for the gas. NGC 2768 is a rare example of an early-type galaxy with detectable CO emission (Wikland et al. 1995) and the host of a calcium-rich supernova type Ib (Filippenko & Chornock 2000). The effective radius of the galaxy is 1.06 arcmin (Proctor et al. 2009; Cappellari et al. 2011). For a distance of 21.8 Mpc (Cappellari et al. 2011), this corresponds to 6.7 kpc.

2 KINEMATIC TRACERS

2.1 Galaxy starlight data

Using a new technique to extract integrated kinematic information of the underlying galaxy starlight from a multi-slit spectrograph, Proctor et al. (2009) presented 2D stellar kinematics for NGC 2768 out to ∼3 R_e. Here we have carried out a re-analysis of the Proctor et al. galaxy data after re-defining the sky scaling index continuum passbands to avoid any strong spectral features associated with the galaxy, as well as any skylines in order to refine the sky subtraction (see Foster et al. 2009 for more details). The resulting velocity and velocity dispersion profiles are similar to those published in Proctor et al. (2009). The total number of positions with stellar kinematics available is 104 and our full data set is given in Table A1 of Appendix A.

2.2 Planetary nebulae (PNe) data

Velocity data for 315 PNe in NGC 2768 were acquired using the PN.S spectrograph (Douglas et al. 2002) in 2007 and are available at www.strw.leidenuniv.nl/pns/. Details of the data reduction procedure and analysis can be found in Cortesi et al. (2012, in preparation). Following Coccato et al. (2009), a uniform magnitude cut has been applied and radial incompleteness tests have been carried out. Thus each bin of the PNe surface density distribution is complete to a given magnitude and has been statistically corrected for any radial incompleteness. All are spectroscopically confirmed. The PNe data reach out to ∼5 R_e.

2.3 Globular cluster (GC) data

The radial surface density distribution and velocity data for GCs come from the imaging and spectroscopy of Pota et al. (2012). Briefly, imaging from *Hubble Space Telescope (HST)* allows us to model and subtract the galaxy light, and hence detect GCs in the galaxy inner regions with little or no radial incompleteness. The resulting surface density distribution for over 500 GCs is a combination of *HST* data in the inner regions and Subaru data in the outer regions, with a background level subtracted. Blue and red GCs were separated according to the local minimum of their bimodal colour distribution, i.e. at $R - z = 0.56$ (Pota et al. 2012).

Follow-up Keck spectroscopy returned 112 kinematically confirmed blue and red GCs (Pota et al. 2012). The blue GCs, associated with galaxy haloes (Forbes et al. 2012), were not found to rotate (Pota et al. 2012). Here we only consider further the 62 GCs from the red subpopulation. For these GCs the mean velocity is 1353 ± 3 km s^{-1} in excellent agreement with the galaxy systemic velocity of 1353 km s^{-1} (Cappellari et al. 2011). The red GCs reach out to ∼4 R_e and we henceforth assume that they are all associated with the bulge of the galaxy.

3 RESULTS AND DISCUSSION

3.1 Spatial distributions

The locations of the 481 starlight, PNe and red GC positions with kinematic data in NGC 2768 are shown in Fig. 1. The kinematic data points are well distributed across the surface of the galaxy. In some cases the GC and starlight velocities come from the same position on the sky.
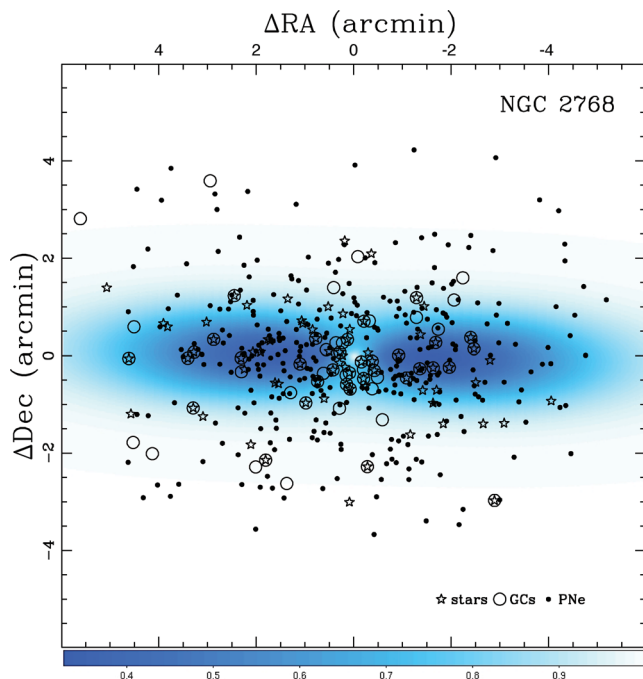
Figure 1. Distribution of planetary nebulae (PNe, solid dots), red globular clusters (GCs, open circles) and starlight positions (stars) for which velocity information is available for NGC 2768. Also shown is a grey-scale corresponding to the probability of association with the bulge component (high values in the grey-scale bar shown below). The effective radius of the galaxy is 1.06 arcmin.

Before examining the kinematic data, we compare the 1D radial distribution of the PNe and red GCs with the galaxy starlight. We use the results of the starlight decomposition into bulge and disc components from Cortesi et al. (2012, in preparation). The general method is to create a model that can be used to assign a probability that a given position is associated with either the disc or bulge component as described in Cortesi et al. (2011). Briefly, it involves a 2D decomposition of a K-band image of NGC 2768 from the Two Micron All Sky Survey (2MASS) survey. From this, parameters for the disc and bulge, assuming an exponential and Sérsic light profile, respectively, are obtained. The resulting major axis scale lengths, Sérsic indices, K-band magnitudes and axial ratios are given in Table 1. The 2D disc/bulge probability map is shown in Fig. 1.

The bulge has a position angle that is consistent with the major axis of the disc. We also find the bulge and disc to have similar scale sizes. Using a distance of 21.8 Mpc and the K-band magnitudes quoted in Table 1 (assuming a solar value of $K = 3.28$) we can calculate the luminosity in each component. To calculate masses, we need to assume a mass-to-light ratio that depends on both age and metallicity. The advantage of working in the K band is that it is relatively insensitive to metallicity and we simply assume solar. In a study of age gradients in S0 galaxies, Bedregal et al. (2011)

Table 1. Bulge-to-disc decomposition of NGC 2768.

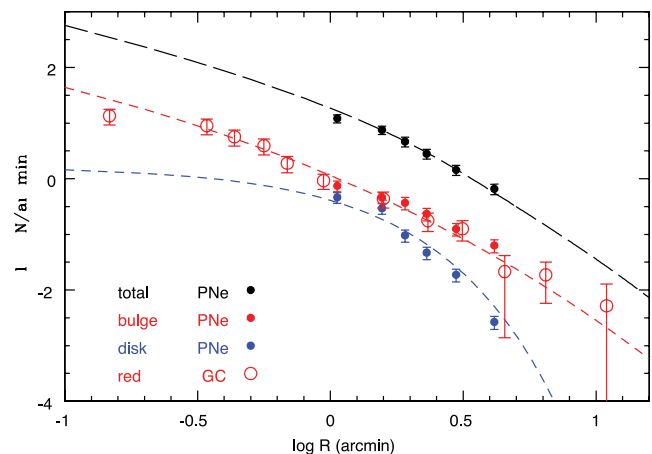| Parameter	Disc	Bulge
$R_{\rm d}$, $R_{\rm e}$ (arcmin)	0.72	0.84
Sérsic n	$\equiv 1$	4.65
K (mag)	8.19	7.23
b/a	0.29	0.66

Figure 2. Surface density of planetary nebulae (PNe) and globular clusters (GCs) in NGC 2768 as a function of the galaxy major axis. The surface density of red GCs is shown as red open circles. The surface density of PNe assigned to the disc and bulge components is shown as blue and red dots, respectively. The combined total PNe surface density is shown as black dots. The disc, bulge and total galaxy starlight profiles from a bulge-to-disc decomposition are given as blue, red and black dashed lines. The normalization in the vertical direction is arbitrary (i.e. the disc and bulge distributions have been offset for clarity; in reality the bulge dominates at small and large radii). A good correspondence is seen between the bulge PNe, bulge starlight and red GCs.

found age gradients to be positive (with discs younger than bulges) or flat. The typical mean age was around 5 Gyr. Although NGC 2768 shows some indication of recent star formation (e.g. a type Ib supernova in 2000), we assume that a mean age of 5 Gyr is more appropriate. The mass-to-light ratio in the K band for a near solar 5 Gyr population is 0.6 (e.g. Forbes et al. 2008). This gives the mass of the disc to be $3.1 \times 10^{10} \, \rm M_{\odot}$ and $7.5 \times 10^{10} \, \rm M_{\odot}$ for the bulge. Thus the bulge-to-total mass ratio is 0.7.

Fig. 2 shows the 1D radial surface density distribution of disc and bulge PNe and the red (bulge) GCs with the galaxy starlight profiles. The radial bins, using geometric circular radii, are chosen to have similar numbers of objects in each bin with Poisson errors shown. Our assumption of associating the red GCs with the bulge is supported by the similarity between their surface density profile and that of the bulge starlight.

3.2 Kinematic profiles

We next explore the radial kinematic (rotation velocity and dispersion) profiles of our three tracers. For the PNe we follow the method of Cortesi et al. (2011) which calculates the disc and bulge kinematics separately in probability-weighted radial bins, with disc/bulge probabilities taken from our spatial analysis. A likelihood clipping is employed to reject data points that are more than $\sim 2\sigma$ from either the disc or the bulge model, leaving 289 PNe data points. The model fits for rotation velocity and velocity dispersion with only the minimal assumption that the line-of-sight velocity distributions for the disc and bulge are drawn from Gaussians.

Conducting a similar disc/bulge analysis on the red GCs revealed that none were assigned to the disc with more than 68 per cent confidence. This, along with our finding that the surface density of the red GCs follows that of the bulge starlight (Fig. 2), supports our assumption that the red GCs probe the bulge component only.

Thus for the kinematic modelling all of the red GCs are assigned to the bulge.

Unlike our two discrete tracers, the starlight data are integrated quantities for which the rotation velocity and velocity dispersion come directly from the measurements. Ideally, with full wavelength coverage and a high signal-to-noise 2D spectrum we could attempt to decompose the starlight into disc and bulge components (Johnston et al. 2012). However for our data, which are modest signal-to-noise data from a restricted wavelength range around the Ca triplet lines, we adopt a simpler approach. We assign each starlight position to *either* the disc or the bulge based on the probability map of Fig. 1. The rotation amplitude is fit by an inclined disc model rotating along the major axis using equation 3 from Foster et al. (2011) which fits the rotation velocity and velocity dispersion simultaneously.

In Fig. 3 we show how the starlight and PNe rotation velocity depend on the disc/bulge probability. In both cases the rotation velocity declines smoothly from the disc-dominated regime to the bulge-dominated regime. We note that the velocity dispersion (not shown) does not depend strongly on the disc/bulge probability. The figure also gives the azimuthal dependence on the probability. This shows that low (disc-like) probabilities are exclusively associated with position angles about the major axis (90° and 270°) as expected. For the starlight data we have chosen a probability cut of 63 per cent. This combined with a restriction of velocity errors to be less than $50 \, \mathrm{km \, s^{-1}}$ gives a final sample of 23 disc and 22 bulge-dominated starlight data points. We use these subsamples to calculate the starlight disc and bulge kinematics but recognize that they are still 'contaminated' somewhat by the other component. To explore the sensitivity of this cut, and hence the contamination effect, we have varied the probability by 9 per cent either side of our chosen cut. The resulting systematic change in disc and bulge starlight kinematics is included in our errors.
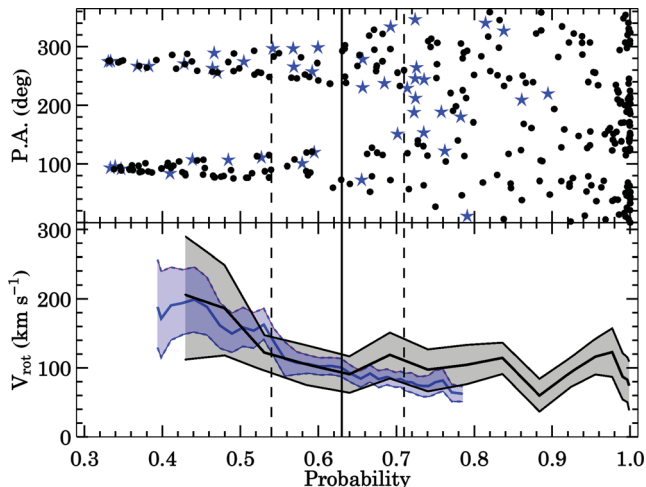

Figure 3. Stellar and PNe rotation velocity of NGC 2768 as a function of the disc/bulge probability. The probability associated with the disc (low values) or the bulge (high values) comes from our bulge-to-disc decomposition of a *K*-band image (see Section 3.1). The *upper* panel shows the position angles of the starlight (stars) and PNe (solid dots) data points, with the galaxy major axis located at ∼90° and 270°. The *lower* panel shows a rolling average of the stellar (blue line) and PNe (black line) rotation velocities and the 1σ confidence limits. The vertical lines at probabilities of 0.63 and ±0.09 indicate our chosen separation between disc (<0.63) and bulge (>0.63) for the starlight data and the range of values that we explore for systematic effects.

In Figs 4 and 5 we show the disc and bulge kinematic profiles from our two-component decomposition. Each radial bin is chosen to have similar numbers in each bin with 289 (disc and bulge) PNe in six radial bins, 122 red (bulge only) GCs in two bins and 45 (disc and bulge) starlight data points in two bins. As detailed above the rotation velocity and velocity dispersion in each radial bin are computed following Cortesi et al. (2011) for the PNe and red GCs and Foster et al. (2011) for the starlight data. For the stellar velocity dispersion we show a continuous profile. We also include the inner region stellar kinematic profiles from the SAURON instrument (Emsellem et al. 2004). For the latter we have simply extracted profiles ±30° about the major and ±60° about the minor axes to approximate the disc and bulge profiles, respectively. The resulting disc and bulge data are both plotted as a function of a generalized radius, i.e.

$$R = \sqrt{R_{\mathrm{maj}}^2 q + R_{\mathrm{min}}^2/q}, \tag{1}$$

where R_{maj} is the semi-major axis, R_{min} is the semi-minor axis and q is the axial ratio of 0.46 from 2MASS.

Figs 4 and 5 shows generally good agreement between the PNe kinematics and the kinematics probed by red GCs and direct starlight to large radii for NGC 2768. We also see reasonable consistency in the inner regions with the SAURON stellar kinematic data. We support the earlier work by Cortesi et al. (2011), on the S0 galaxy NGC 1023, finding evidence for distinct populations of disc and bulge PNe.

The disc component reveals a rapid rise reaching a maximum velocity of ∼270 $\mathrm{km \, s^{-1}}$ at a few scale lengths. We note that the true circular velocity may be closer to 311 $\mathrm{km \, s^{-1}}$ given by Davis et al. (2011) from their modelling of molecular gas kinematics which is unaffected by the asymmetric drift that may influence the kinematics derived from stars. Beyond the very inner regions, we find a continuously declining velocity dispersion profile to very low values. In a sample of late-type spiral galaxies, Bottema (1993) found the velocity dispersion to decline exponentially with radius reaching very low values at a few scale lengths. The bulge reveals mild rotation with a near constant velocity of ∼100 $\mathrm{km \, s^{-1}}$ and a mean velocity dispersion of ∼120 $\mathrm{km \, s^{-1}}$ at large radii.

Fig. 4 also shows that V_{rot}/σ for the disc rises continuously with radius. Such a trend suggests that NGC 2768 could be descended from a galaxy with an extended disc. The simulations of Bournaud et al. (2005) showed that such high values of V_{rot}/σ are maintained after a minor merger. Minor mergers may also help to build up the bulge mass. We note that an isotropic oblate rotator of $b/a =$ 0.66 (see Table 1) would be expected to have $V_{\mathrm{rot}}/\sigma \sim 0.7$ (Davies et al. 1983), similar to our average value. The bulge of NGC 2768 (Fig. 5) resembles a pressure-supported system similar to those seen for the bulges of other spiral galaxies (MacArthur, González & Courteau 2009). Thus we find NGC 2768 to have kinematic properties that resemble those of a spiral galaxy (although with a dominant bulge). We note that determining the exact differences and testing the various evolutionary processes suggested for S0 formation would require a detailed analysis beyond the scope of this paper.

4 CONCLUSIONS

By combining galaxy starlight, PNe and red GC data for NGC 2768 we have shown that the red subpopulation of GCs and a subpopulation of PNe follow the same radial surface density profile as the bulge component of the galaxy starlight. An additional distinct,
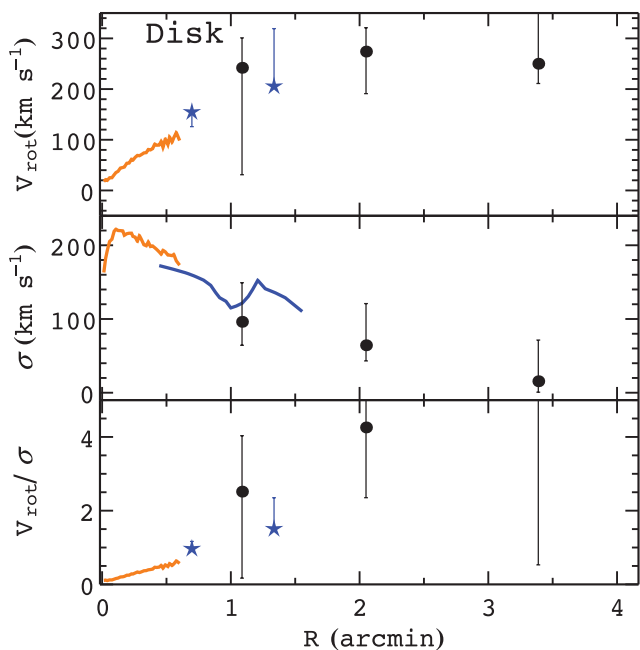
Figure 4. Disc kinematic profiles for NGC 2768. Symbols are solid dots for PNe, open circles for GCs and blue stars for starlight data. The stellar velocity dispersion is shown as a continuous blue line. The continuous orange lines at small radii show the SAURON data along the major (disc) and minor (bulge) axes. The *upper* panels show the rotation velocity (V_{rot}), the *middle* panels the velocity dispersion (σ) and the *lower* panels the V_{rot}/σ ratio (note the different scales on the *left*- and *right*-hand sides). The outermost disc V_{rot}/σ data point is off scale. The *x*-axis shows the generalized radius as given by equation (1). Generally good agreement is seen between the different kinematic tracers.
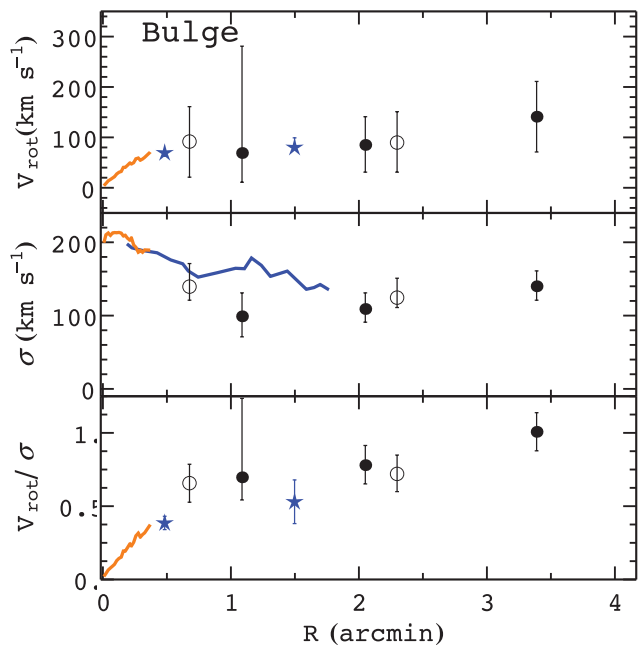

Figure 5. Bulge kinematic profiles for NGC 2768. Symbols are the same as Fig. 4. The continuous orange lines at small radii show the SAURON data along the major (disc) and minor (bulge) axes. The *upper* panels show the rotation velocity (V_{rot}), the *middle* panels the velocity dispersion (σ) and the *lower* panels the V_{rot}/σ ratio (note the different scales on the *left*- and *right*-hand sides). The *x*-axis shows the generalized radius as given by equation 1. Generally good agreement is seen between the different kinematic tracers.

and presumably younger, PNe subpopulation is associated with the galaxy disc.

We have also investigated the radially extended kinematics of these three tracers out to ~4 R_e and show that they are in very good agreement with each other over a large range of radii. Using a 2D probability map generated from a *K*-band bulge-to-disc decomposition we estimate the bulge-to-total ratio to be 0.7, with both components having a similar scale size. Using this two-component decomposition we examined the kinematics of the bulge and disc separately finding that the disc component reveals rapid rotation and a falling velocity dispersion profile resulting in an increasing V_{rot}/σ ratio with radius. Such a behaviour is similar to that seen in the discs of late-type spiral galaxies. We also found a slowly rotating bulge, indicative of a pressure-supported system.

Although NGC 2768 is an S0 galaxy, many elliptical galaxies contain embedded discs and potentially an associated subpopulation of disc PNe. This work shows that bulge and disc components may need to be taken into account in any kinematic, or mass, analysis of early-type galaxies. This is particularly true when using kinematics to help unravel the origin of S0 galaxies.

REFERENCES

Aragón-Salamanca A., Bedregal A. G., Merrifield M. R., 2006, A&A, 458, 101
Bedregal A. G., Aragón-Salamanca A., Merrifield M. R., 2006, MNRAS, 373, 1125
Bedregal A. G., Cardiel N., Aragón-Salamanca A., Merrifield M. R., 2011, MNRAS, 415, 2063
Bottema R., 1993, A&A, 275, 16
Bournaud F., Jog C. J., Combes F., 2005, A&A, 437, 69
Brodie J. P., Strader J., 2006, ARA&A, 44, 193
Cappellari M. et al., 2011, MNRAS, 413, 813
Ciardullo R., Sigurdsson S., Feldmeier J. J., Jacoby G. H., 2005, ApJ, 629, 499
Coccato L. et al., 2009, MNRAS, 394, 1249
Coccato L., Arnaboldi M., Gerhard O., Freeman K., Ventimiglia G., Yasuda N., 2010, A&A, 519, 95
Cortesi A. et al., 2011, MNRAS, 414, 642
Côté P., 1999, AJ, 118, 406
Davies R. L., Efstathiou G., Fall S. M., Illingworth G., Schechter P. L., 1983, ApJ, 266, 41
Davis T. et al., 2011, MNRAS, 414, 968
Dekel A., Stoehr F., Mamon G. A., Cox T. J., Novak G. S., Primack J. R., 2005, Nat, 437, 707
Douglas N. G. et al., 2002, PASP, 114, 1234
Dressler A., 1980, ApJ, 236, 351
Emsellem E. et al., 2004, MNRAS, 352, 721
Filippenko A., Chornock R., 2000, IAU Circ., 7511, 2
Forbes D. A., Brodie J. P., Larsen S., 2001, ApJ, 556, L83
Forbes D. A., Lasky P., Graham A., Spitler L., 2008, MNRAS, 389, 1924
Forbes D. A., Ponman T., O'Sullivan E., 2012, MNRAS, 425, 66
Forte J. C., Faifer F., Geisler D., 2005, MNRAS, 357, 56

Foster C., Proctor R. N., Forbes D. A., Spolaor M., Hopkins P. F., Brodie J. P., 2009, MNRAS, 400, 2135

Foster C. et al., 2011, MNRAS, 415, 3393

Fried J. W., Illingworth G. D., 1994, AJ, 107, 992

Garcia A., 1993, A&AS, 100, 47

Hurley-Keller D., Morrison H. L., Harding P., Jacoby G. H., 2004, ApJ, 616, 804

Johnston E., Aragón-Salamanca, Merrifield M., Bedregal A., 2012, MNRAS, 422, 2590

Kim D., 1989, ApJ, 346, 653

Kormendy J., Bender R., 2012, ApJS, 198, 2

MacArthur L. A., González J. J., Courteau S., 2009, MNRAS, 395, 28

Minniti D., 1995, A&A, 303, 468

Nolthenius R., Ford H. C., 1987, ApJ, 317, 62

Pota V. et al., 2012, MNRAS, (submitted)

Proctor R. N., Forbes D. A., Romanowsky A. J., Brodie J. P., Strader J., Spolaor M., Mendel J. T., Spitler L., 2009, MNRAS, 398, 91

Romanowsky A. J., Douglas N. G., Arnaboldi M., Kuijken K., Merrifield M. R., Napolitano N. R., Capaccioli M., Freeman K. C., 2003, Sci., 301, 1696

Romanowsky A. J., Fall M., 2012, ApJS, in press

Sandage A., Tammann G. A., van den Bergh S., 1981, J. R. Astron. Soc. Canada, 75, 267

Strader J. et al., 2011, ApJS, 197, 33

Weijmans A.-M. et al., 2009, MNRAS, 398, 561

Wikland T., Combes F., Henkel C., 1995, A&A, 297, 643

Wilman D. J., Oemler A., Jr, Mulchaey J. S., McGee S. L., Balogh M. L., Bower R. G., 2009, ApJ, 692, 298

APPENDIX A:

Table A1. Galaxy kinematic data. Columns 1 and 2 give the position in right ascension and declination (J2000), respectively. Columns 3 and 4 give the galactocentric radius. The measured kinematic moments are given in columns 5–8. The data for two individual masks are included (Y and Z); however, mask Y has been observed twice independently and is labelled Y1 and Y2.

α (hh:mm:ss)	δ (°:′:″)	r (arcsec)	PA (deg)	V_{obs} (km s^{-1})	σ (km s^{-1})	h_3	h_4
(1)	(2)	(3)	(4)	(5)	(6)	(7)	(8)
				Mask Y1			
09:11:28.703	60:02:48.06	92.5	297	1205 ± 11	143 ± 18	0.08 ± 0.09	−0.02 ± 0.12
09:11:39.886	60:01:37.87	81.5	153	1343 ± 14	178 ± 19	−0.02 ± 0.06	0.02 ± 0.09
09:11:20.931	60:02:07.85	126.4	267	1148 ± 8	126 ± 12	0.01 ± 0.07	−0.12 ± 0.13
09:11:23.223	60:02:24.78	106.9	275	1122 ± 7	107 ± 18	0.07 ± 0.07	0.10 ± 0.08
09:11:33.407	60:02:16.73	29.9	273	1228 ± 5	171 ± 8	0.02 ± 0.02	0.01 ± 0.02
09:11:25.877	60:03:16.79	152.8	306	1209 ± 55	110 ± 65	0.05 ± 0.09	−0.03 ± 0.13
09:11:24.979	60:01:32.49	137.4	245	1218 ± 15	113 ± 20	0.06 ± 0.07	−0.08 ± 0.10
09:11:22.204	60:02:08.74	116.5	267	1127 ± 9	96 ± 16	0.10 ± 0.08	0.05 ± 0.13
09:11:28.835	60:01:58.20	77.1	255	1217 ± 8	142 ± 10	0.03 ± 0.05	0.01 ± 0.05
09:11:30.367	60:02:41.56	74.4	297	1240 ± 7	130 ± 11	−0.02 ± 0.06	−0.05 ± 0.06
09:11:19.758	60:01:45.71	152.5	257	1197 ± 13	123 ± 11	−0.01 ± 0.05	−0.06 ± 0.07
09:11:21.916	60:00:13.79	297.6	224	1306 ± 123	211 ± 117	0.01 ± 0.07	−0.02 ± 0.10
09:11:38.854	60:02:07.47	19.2	125	1376 ± 5	196 ± 8	0.01 ± 0.01	−0.02 ± 0.03
09:11:36.253	60:01:59.28	36.3	208	1309 ± 5	180 ± 8	0.00 ± 0.02	0.02 ± 0.02
09:11:37.409	60:01:32.92	91.8	180	1314 ± 22	212 ± 26	−0.12 ± 0.08	0.07 ± 0.17
09:11:35.694	60:02:12.86	14.2	260	1270 ± 5	203 ± 8	0.03 ± 0.01	0.01 ± 0.02
09:11:19.269	60:03:04.43	165.7	290	1152 ± 70	65 ± 84	0.08 ± 0.10	0.01 ± 0.16
09:11:41.096	60:01:58.14	44.3	122	1400 ± 5	174 ± 8	−0.04 ± 0.02	0.02 ± 0.06
09:11:24.573	59 59 56.42	324.5	215	1132 ± 85	106 ± 54	0.00 ± 0.06	−0.03 ± 0.06
09:11:34.314	60:01:54.53	52.3	228	1274 ± 5	155 ± 8	0.00 ± 0.02	0.01 ± 0.03
09:11:39.822	60:02:19.25	21.0	77	1403 ± 5	194 ± 8	−0.02 ± 0.01	0.00 ± 0.02
09:11:31.048	60:02:31.14	56.5	289	1221 ± 6	172 ± 9	0.04 ± 0.04	0.05 ± 0.04
09:11:36.752	60:01:38.21	80.9	187	1329 ± 16	184 ± 20	−0.08 ± 0.07	0.02 ± 0.12
09:11:19.078	60:01:59.02	145.3	263	1136 ± 13	91 ± 28	0.17 ± 0.08	0.00 ± 0.12
09:12:10.561	60:01:39.79	254.6	98	1329 ± 144	170 ± 144	0.02 ± 0.08	−0.02 ± 0.12
09:12:02.699	59 59 31.30	388.4	131	1325 ± 164	228 ± 153	0.01 ± 0.11	0.00 ± 0.19
09:11:59.927	60:02:23.17	172.0	87	1560 ± 53	131 ± 102	−0.01 ± 0.10	0.05 ± 0.12
09:11:59.744	60:01:04.39	217.6	113	1481 ± 79	164 ± 107	−0.05 ± 0.06	−0.01 ± 0.05
09:11:57.921	60:01:54.50	157.0	98	1500 ± 27	149 ± 63	−0.12 ± 0.11	0.03 ± 0.12
09:11:57.142	60:02:35.58	158.9	82	1506 ± 45	125 ± 86	−0.09 ± 0.10	−0.05 ± 0.12
09:11:56.449	60:02:48.83	166.7	77	1523 ± 47	148 ± 87	−0.01 ± 0.12	−0.07 ± 0.11
09:11:53.358	60:02:10.14	119.7	92	1523 ± 11	127 ± 15	−0.14 ± 0.06	−0.07 ± 0.12
09:11:53.195	60:01:00.13	193.0	122	1289 ± 41	168 ± 65	−0.01 ± 0.06	0.00 ± 0.04
09:11:51.588	60:01:40.84	124.7	108	1445 ± 19	159 ± 18	−0.18 ± 0.05	−0.09 ± 0.11

Table A1 – *continued*

α (hh:mm:ss) (1)	δ (°: :) (2)	r (arcsec) (3)	PA (deg) (4)	V_{obs} (km s^{-1}) (5)	σ (km s^{-1}) (6)	h_3 (7)	h_4 (8)
09:11:50.723	60:02:07.76	100.2	94	1500 ± 9	141 ± 12	−0.07 ± 0.04	0.01 ± 0.09
09:11:49.342	60:01:38.98	114.1	112	1456 ± 15	175 ± 16	−0.11 ± 0.04	0.00 ± 0.10
09:11:48.534	60:02:05.28	84.7	97	1490 ± 8	155 ± 8	−0.11 ± 0.03	−0.06 ± 0.07
09:11:48.180	60:02:46.95	111.1	69	1460 ± 22	141 ± 57	0.04 ± 0.07	0.08 ± 0.08
09:11:46.500	60:01:52.47	80.8	108	1457 ± 7	152 ± 8	−0.05 ± 0.03	−0.09 ± 0.05
09:11:44.879	60:02:19.45	57.9	86	1463 ± 6	167 ± 8	−0.06 ± 0.02	−0.04 ± 0.04
09:11:17.066	60:03:14.92	191.6	291	1131 ± 102	33 ± 114	0.03 ± 0.09	−0.03 ± 0.11
09:11:14.309	60:02:18.90	173.3	271	1182 ± 20	98 ± 31	0.10 ± 0.07	−0.03 ± 0.08
09:11:13.660	60:00:43.19	279.7	243	1163 ± 97	92 ± 90	0.03 ± 0.06	−0.02 ± 0.12
09:11:12.873	60:02:39.49	187.5	278	1109 ± 40	34 ± 60	0.02 ± 0.07	−0.01 ± 0.06
09:11:11.932	60:00:52.67	273.9	247	1202 ± 76	76 ± 84	0.01 ± 0.07	−0.04 ± 0.10
09:11:11.256	60:02:01.23	201.8	266	1200 ± 34	80 ± 40	0.04 ± 0.06	−0.02 ± 0.07
09:11:10.340	60:01:53.13	213.4	264	1187 ± 55	92 ± 56	0.03 ± 0.07	−0.03 ± 0.11
09:11:01.815	60:00:38.63	354.6	250	1175 ± 116	81 ± 107	0.01 ± 0.07	−0.03 ± 0.12
09:11:00.672	60:01:46.55	288.8	264	1224 ± 93	69 ± 84	−0.01 ± 0.02	−0.01 ± 0.03
09:12:03.148	60:01:07.31	232.9	109	1406 ± 66	247 ± 79	−0.06 ± 0.07	−0.05 ± 0.07
09:10:56.037	60:03:10.99	323.9	280	1194 ± 130	68 ± 117	0.01 ± 0.05	−0.02 ± 0.06
				Mask Y2			
09:11:28.703	60:02:48.06	92.5	297	1209 ± 38	185 ± 48	0.00 ± 0.14	0.09 ± 0.14
09:11:39.886	60:01:37.87	81.5	153	1322 ± 47	191 ± 57	−0.10 ± 0.12	0.10 ± 0.27
09:11:20.931	60:02:07.85	126.4	267	1140 ± 25	110 ± 45	0.05 ± 0.13	0.11 ± 0.12
09:11:23.223	60:02:24.78	106.9	275	1127 ± 25	132 ± 45	0.08 ± 0.12	0.08 ± 0.11
09:11:33.407	60:02:16.73	29.9	273	1232 ± 5	179 ± 8	0.00 ± 0.04	0.00 ± 0.03
09:11:25.877	60:03:16.79	152.8	306	1217 ± 113	151 ± 117	0.05 ± 0.11	−0.03 ± 0.14
09:11:24.979	60:01:32.49	137.4	245	1200 ± 98	244 ± 743	−0.15 ± 0.12	0.07 ± 0.12
09:11:22.204	60:02:08.74	116.5	267	1127 ± 27	102 ± 51	0.08 ± 0.14	0.08 ± 0.13
09:11:28.835	60:01:58.20	77.1	255	1216 ± 25	171 ± 29	−0.06 ± 0.10	−0.03 ± 0.09
09:11:30.367	60:02:41.56	74.4	297	1227 ± 19	157 ± 23	0.01 ± 0.11	−0.02 ± 0.09
09:11:19.758	60:01:45.71	152.5	257	1187 ± 60	145 ± 66	−0.02 ± 0.10	−0.04 ± 0.10
09:11:38.854	60:02:07.47	19.2	125	1378 ± 5	210 ± 8	0.00 ± 0.02	0.04 ± 0.05
09:11:36.253	60:01:59.28	36.3	208	1310 ± 6	184 ± 9	−0.03 ± 0.03	0.03 ± 0.07
09:11:37.409	60:01:32.92	91.8	180	1293 ± 144	321 ± 113	−0.10 ± 0.12	0.20 ± 0.19
09:11:35.694	60:02:12.86	14.2	260	1273 ± 5	203 ± 8	0.01 ± 0.01	−0.03 ± 0.05
09:11:19.269	60:03:04.43	165.7	290	1148 ± 143	55 ± 119	0.12 ± 0.11	0.00 ± 0.14
09:11:41.096	60:01:58.14	44.3	122	1400 ± 8	169 ± 15	−0.05 ± 0.04	0.01 ± 0.08
09:11:34.314	60:01:54.53	52.3	228	1274 ± 10	176 ± 12	−0.04 ± 0.06	0.04 ± 0.11
09:11:39.822	60:02:19.25	21.0	77	1404 ± 5	190 ± 8	−0.03 ± 0.02	−0.01 ± 0.03
09:11:31.048	60:02:31.14	56.5	289	1226 ± 13	166 ± 15	0.03 ± 0.08	−0.01 ± 0.07
09:11:36.752	60:01:38.21	80.9	187	1311 ± 73	300 ± 76	−0.06 ± 0.10	0.19 ± 0.19
09:11:19.078	60:01:59.02	145.3	263	1149 ± 38	82 ± 64	0.03 ± 0.13	−0.01 ± 0.14
09:11:59.927	60:02:23.17	172.0	87	1523 ± 153	96 ± 129	0.04 ± 0.11	−0.09 ± 0.11
09:11:59.744	60:01:04.39	217.6	113	1346 ± 148	148 ± 117	−0.01 ± 0.08	0.01 ± 0.07
09:11:57.921	60:01:54.50	157.0	98	1488 ± 85	172 ± 118	−0.14 ± 0.13	0.05 ± 0.16
09:11:57.142	60:02:35.58	158.9	82	1481 ± 91	149 ± 144	0.10 ± 0.12	−0.10 ± 0.12
09:11:56.449	60:02:48.83	166.7	77	1621 ± 160	223 ± 114	0.10 ± 0.08	−0.01 ± 0.09
09:11:53.358	60:02:10.14	119.7	92	1526 ± 34	114 ± 69	−0.12 ± 0.14	−0.14 ± 0.20
09:11:53.195	60:01:00.13	193.0	122	1398 ± 125	150 ± 118	0.03 ± 0.04	−0.01 ± 0.03
09:11:51.588	60:01:40.84	124.7	108	1466 ± 34	148 ± 58	−0.12 ± 0.11	0.02 ± 0.22
09:11:50.723	60:02:07.76	100.2	94	1477 ± 25	286 ± 49	−0.11 ± 0.10	0.25 ± 0.38
09:11:49.342	60:01:38.98	114.1	112	1437 ± 25	160 ± 43	−0.09 ± 0.09	0.04 ± 0.16
09:11:48.534	60:02:05.28	84.7	97	1485 ± 20	166 ± 36	−0.12 ± 0.08	0.00 ± 0.18
09:11:48.180	60:02:46.95	111.1	69	1457 ± 40	197 ± 75	0.08 ± 0.10	0.07 ± 0.09
09:11:46.500	60:01:52.47	80.8	108	1465 ± 16	155 ± 33	−0.08 ± 0.07	0.03 ± 0.15
09:11:44.879	60:02:19.45	57.9	86	1460 ± 9	172 ± 18	−0.05 ± 0.05	0.00 ± 0.08
09:11:17.066	60:03:14.92	191.6	291	1264 ± 126	118 ± 144	0.02 ± 0.10	−0.05 ± 0.12
09:11:14.309	60:02:18.90	173.3	271	1237 ± 82	225 ± 76	0.11 ± 0.09	0.03 ± 0.12
09:11:12.873	60:02:39.49	187.5	278	1197 ± 128	122 ± 120	0.04 ± 0.09	0.02 ± 0.11
09:11:11.256	60:02:01.23	201.8	266	1132 ± 115	28 ± 122	−0.01 ± 0.04	−0.01 ± 0.03
09:11:10.340	60:01:53.13	213.4	264	1215 ± 39	123 ± 60	0.01 ± 0.07	−0.03 ± 0.07
09:11:05.861	60:02:33.21	237.2	274	1099 ± 170	135 ± 107	−0.05 ± 0.08	0.01 ± 0.10
09:12:35.618	59 58:53.58	591.3	115	1382 ± 99	38 ± 102	−0.01 ± 0.03	−0.02 ± 0.03

Table A1 – *continued*

α (hh:mm:ss) (1)	δ (°: :) (2)	r (arcsec) (3)	PA (degree) (4)	V_{obs} (km s^{-1}) (5)	σ (km s^{-1}) (6)	h_3 (7)	h_4 (8)
09:11:06.573	60:02:29.59	231.4	274	1173 ± 173	49 ± 136	0.03 ± 0.09	−0.01 ± 0.09
09:10:56.037	60:03:10.99	323.9	280	1227 ± 163	76 ± 129	0.01 ± 0.09	−0.01 ± 0.10
				Mask Z			
09:11:31.966	60:01:38.66	92.4	228	1305 ± 11	140 ± 15	0.15 ± 0.05	0.02 ± 0.13
09:11:28.467	60:02:51.46	98.9	298	1256 ± 9	157 ± 12	0.08 ± 0.05	−0.01 ± 0.07
09:11:35.293	60:02:03.77	30.6	234	1290 ± 5	181 ± 8	0.03 ± 0.01	0.00 ± 0.03
09:11:38.698	60:02:57.40	93.1	13	1357 ± 14	138 ± 26	−0.02 ± 0.07	−0.06 ± 0.07
09:11:25.602	60:01:31.53	135.6	244	1292 ± 32	169 ± 42	0.15 ± 0.11	−0.03 ± 0.19
09:11:32.622	60:03:11.46	124.3	328	1301 ± 20	148 ± 26	0.00 ± 0.06	0.02 ± 0.06
09:11:39.464	60:01:47.13	61.5	151	1354 ± 5	143 ± 8	−0.02 ± 0.03	0.00 ± 0.03
09:11:33.276	60:01:18.27	130.1	208	1328 ± 20	140 ± 26	−0.02 ± 0.06	−0.07 ± 0.07
09:11:37.061	60:01:52.67	49.2	186	1336 ± 5	154 ± 8	−0.02 ± 0.02	0.05 ± 0.08
09:11:40.642	60:02:09.32	26.5	104	1426 ± 5	179 ± 8	−0.02 ± 0.01	−0.02 ± 0.01
09:11:35.163	60:03:04.31	106.5	341	1315 ± 13	124 ± 16	−0.03 ± 0.06	−0.08 ± 0.10
09:11:30.339	60:01:11.08	153.4	220	1310 ± 25	140 ± 33	0.06 ± 0.08	−0.09 ± 0.17
09:11:35.188	60:02:16.80	16.7	276	1271 ± 5	196 ± 8	0.02 ± 0.01	−0.01 ± 0.05
09:11:36.263	60:02:33.27	39.4	335	1311 ± 5	187 ± 8	0.02 ± 0.01	0.02 ± 0.02
09:11:36.492	60:02:45.93	66.5	348	1318 ± 5	153 ± 11	0.02 ± 0.03	0.07 ± 0.06
09:11:28.833	60:01:58.16	77.2	255	1241 ± 8	148 ± 8	0.04 ± 0.05	−0.12 ± 0.22
09:11:23.563	60:02:23.41	104.1	275	1153 ± 12	106 ± 23	0.11 ± 0.12	−0.02 ± 0.25
09:11:51.197	60:01:24.50	144.5	116	1459 ± 47	186 ± 81	0.01 ± 0.11	0.01 ± 0.08
09:11:50.773	60:02:39.11	117.4	77	1466 ± 36	158 ± 62	−0.05 ± 0.12	0.02 ± 0.12
09:11:48.366	60:03:22.15	173.5	51	1370 ± 131	197 ± 127	0.03 ± 0.12	0.04 ± 0.11
09:11:48.434	60:06:57.22	625.4	16	1464 ± 189	461 ± 161	−0.12 ± 0.11	0.01 ± 0.14
09:11:47.948	60:00:43.29	208.1	139	1409 ± 165	147 ± 125	−0.09 ± 0.14	0.02 ± 0.13
09:11:46.978	60:03:32.05	187.7	43	1380 ± 110	139 ± 112	0.01 ± 0.13	−0.02 ± 0.11
09:11:41.350	59:59:59.26	294.0	168	1351 ± 173	163 ± 112	−0.02 ± 0.06	0.01 ± 0.07
09:11:38.908	59:59:13.61	393.5	176	1381 ± 220	145 ± 137	−0.04 ± 0.08	−0.01 ± 0.08
09:11:38.953	60:04:21.25	275.1	5	1297 ± 193	166 ± 126	−0.05 ± 0.08	−0.01 ± 0.07
09:11:34.378	60:04:34.25	300.8	351	1300 ± 185	153 ± 131	−0.01 ± 0.08	−0.01 ± 0.08
09:11:41.428	60:07:25.39	677.0	6	1221 ± 211	190 ± 147	−0.05 ± 0.10	−0.06 ± 0.10
09:11:26.564	60:12:28.29	326.6	352	1229 ± 152	108 ± 127	−0.02 ± 0.07	−0.03 ± 0.08

This paper has been typeset from a TEX/LATEX file prepared by the author.